



# Effects of Minor Alloying Elements on Alumina Transformation During the Transient Oxidation of $\beta$ -NiAl

Talia L. Barth<sup>1</sup> · Emmanuelle A. Marquis<sup>1</sup>

Received: 4 October 2020 / Revised: 5 February 2021 / Accepted: 16 February 2021 /  
Published online: 4 April 2021

© The Author(s), under exclusive licence to Springer Science+Business Media, LLC, part of Springer Nature 2021

## Abstract

The transient stage of alumina scale formation on alumina-forming alloys is often accompanied by the formation of metastable  $\text{Al}_2\text{O}_3$  phases that may affect oxidation kinetics and scale microstructure. To clarify the role of dopants on the transient stage of NiAl oxidation, we characterized  $\text{Al}_2\text{O}_3$  scales on a series of oxidized model  $\beta$ -NiAl samples that were un-doped or doped with additions of Ti, Y, Si, Ti + Y, and Si + Y. Our results confirm that different dopant elements (Ti, Si, and Y) have varied effects on the length of transient oxidation of alumina-forming alloys. Ti and Si accelerated the  $\theta$ - to  $\alpha$ - $\text{Al}_2\text{O}_3$  transformation via two different mechanisms. Ti promoted  $\alpha$ - $\text{Al}_2\text{O}_3$  nucleation, while Si delayed nucleation but accelerated the lateral growth of the  $\alpha$ - $\text{Al}_2\text{O}_3$  patches. In contrast, Y had little effect on alumina transformation, possibly due to the low Y concentration used in the current study.

**Keywords** NiAl · Oxidation · Phase transformation · Alumina · Scanning electron microscopy (SEM)

## Introduction

Nickel-based alloys are widely used for high-temperature structural applications due to their excellent mechanical properties even at temperatures exceeding 800°C [1, 2]. However, they are also vulnerable to degradation by rapid oxidation at normal use temperatures [3]. To protect against high-temperature oxidation, nickel is often alloyed with aluminum to promote the formation of a protective aluminum oxide ( $\alpha$ - $\text{Al}_2\text{O}_3$ ) surface layer. The  $\alpha$ - $\text{Al}_2\text{O}_3$  phase is preferred because the  $\alpha$ - $\text{Al}_2\text{O}_3$  layer thickens slowly, thus limiting the loss of metal over time [4]. However, the

---

✉ Emmanuelle A. Marquis  
emarq@umich.edu

<sup>1</sup> Department of Materials Science and Engineering, University of Michigan, Ann Arbor, MI, USA

establishment of a continuous protective  $\alpha$ - $\text{Al}_2\text{O}_3$  layer is not an instantaneous process. For oxidation at temperature ranging from 600–1150°C, metastable polymorphs of  $\text{Al}_2\text{O}_3$  often first form during a transient oxidation stage, before transforming into the thermodynamically stable  $\alpha$ - $\text{Al}_2\text{O}_3$  phase [5]. In comparison with the  $\alpha$ - $\text{Al}_2\text{O}_3$  phase, the metastable alumina phases have faster growth rates [6], making them less desirable as protective oxides than the  $\alpha$  phase. Thus, quantifying  $\text{Al}_2\text{O}_3$  transformation kinetics and understanding the factors affecting  $\text{Al}_2\text{O}_3$  transformation rate are of great interest.

$\beta$ -NiAl forms an exclusive alumina scale during oxidation and provides a relevant example of how the metastable to stable alumina phase transformations take place during the initial stages of  $\text{Al}_2\text{O}_3$  scale development. During the early stages of oxidation, metastable  $\gamma$ - $\text{Al}_2\text{O}_3$  or  $\theta$ - $\text{Al}_2\text{O}_3$  forms a uniform, epitaxial layer on the NiAl substrate, with a whisker or blade-like surface morphology indicative of rapid outward growth [7].  $\alpha$ - $\text{Al}_2\text{O}_3$  is thought to nucleate at the oxide–metal interface [8, 9]. The  $\alpha$ - $\text{Al}_2\text{O}_3$  grains then rapidly grow through the thickness of the metastable  $\text{Al}_2\text{O}_3$  layer, and expand laterally through the metastable alumina layer, resulting in circular “patches” visible on the oxide surface [6, 10, 11]. Due to the volume shrinkage that accompanies the phase transformation, radial cracks are often observed at the centers of the  $\alpha$ - $\text{Al}_2\text{O}_3$  patches [5, 10–12]. Upon further oxidation, the patches continue to grow laterally until they impinge upon one another and the alumina layer is transformed entirely to  $\alpha$ - $\text{Al}_2\text{O}_3$ . The complete transformation to  $\alpha$ - $\text{Al}_2\text{O}_3$  coincides with a drastic decrease in the oxidation kinetics [10] as the oxidation rate becomes limited by transport along the  $\alpha$ - $\text{Al}_2\text{O}_3$  grain boundaries [13]. The length of the transient stage depends on a number of factors, including oxidation temperature, surface finish, and alloy composition [14].

Different alloying additions have been found to affect the rate of the alumina transformation to a fully  $\alpha$ - $\text{Al}_2\text{O}_3$  scale during thermal oxidation. Additions of Y have been found to delay the alumina transformation [12, 15–17], while Ti additions may accelerate the transformation and reduce the length of the transient oxidation stage [15, 18, 19]. Similarly, Si additions are thought to accelerate the transformation to  $\alpha$ - $\text{Al}_2\text{O}_3$  [20, 21]. The overall rate of transformation is a convolution of the nucleation and lateral growth rates of  $\alpha$ - $\text{Al}_2\text{O}_3$  patches, and whether dopants affect one or both mechanisms remains unknown. Yet, such mechanistic understanding is needed for the design of alloys that rapidly form protective  $\alpha$ - $\text{Al}_2\text{O}_3$  layers over a range of temperatures [22], and to develop models of alumina growth kinetics that take transient oxidation into account [23, 24].

To clarify the role of dopants on the transient stage of NiAl oxidation, we characterized the microstructures of the  $\text{Al}_2\text{O}_3$  scales on a series of oxidized  $\beta$ -NiAl samples that were un-doped or doped with additions of Ti, Y, Si, Ti+Y, and Si+Y. Emphasis was placed on determining which aspects of the transient stage of alumina development on NiAl these dopants affect.

## Experimental Details

A single-phase  $\beta$ -NiAl alloy was selected with additions of Ti, Y, and Si to understand the effects of different “reactive” elements, and additional alloys containing combinations of Ti + Y and Si + Y to ascertain any effect of co-doping. Six alloys with nominal compositions listed in Table 1 were obtained from the Ames Laboratory Material Preparation Center, where they were arc-melted and cast into cylindrical rods. The as-received alloys were sectioned, homogenized at 1200°C in argon gas for at least 20 h, and subsequently quenched in water. Prior to oxidation, samples were ground with SiC paper using successively finer grit steps through 1200 grit, then polished with 3 and 1  $\mu\text{m}$  diamond slurries. A final polishing step was performed with colloidal silica. Samples were ultrasonically cleaned in ethanol between each consecutive grinding and polishing step. The as-annealed alloys were polycrystalline, with grain sizes ranging from 50 to 300  $\mu\text{m}$ .

Because NiAl grain orientation can have a significant effect on metastable alumina growth and transformation [25–27], care was taken to compare grains of the same orientation for each alloy at successive oxidation times. Prior to oxidation, electron back scatter diffraction (EBSD) mapping of each sample was performed using a TESCAN MIRA3 FEG scanning electron microscope (SEM) equipped with an EDAX Hikari Camera for EBSD. Sample surfaces were tilted to 70° for data collection, and EBSD maps were obtained for each alloy at 30 keV.

For the short-term isothermal oxidation experiments, polished samples were placed in an alumina boat inside a quartz tube furnace. The furnace was heated to 950°C in flowing Ar, and then samples were moved into the hot zone of the furnace, where they reached a steady temperature in approximately 1–2 min. Once the samples reached 950°C, flowing 20% O<sub>2</sub>-Ar gas was introduced and samples were oxidized for times ranging from 1 to 15 h before quenching in air. After initial observations, additional isothermal oxidation experiments were performed for 25 h for the Ti-, Si- and co-doped alloys, and 50 h for the Y- and un-doped alloys.

Several techniques were used for phase identification, microstructure characterization, and chemical mapping. Photo-stimulated luminescence spectroscopy (PSLS) was used to identify the alumina phases present in the transient oxidation experiments [11, 28, 29]. PSLS mapping and correlative SEM imaging were done using a TESCAN RISE scanning electron microscope (SEM) equipped with a WITec RISE Confocal Raman microscope. Imaging was done at 10 keV, and PSLS was performed

**Table 1** Nominal alloy compositions in at.%

ID	Ni	Al	Ti	Y	Si
NiAl	bal	42	0	0	0
NiAlTi	bal	42	1	0	0
NiAlY	bal	42	0	0.05	0
NiAlSi	bal	42	0	0	0.5
NiAlTiY	bal	42	1	0.05	0
NiAlSiY	bal	42	0	0.05	0.5

using a 532 nm laser. Surface imaging after the oxidation experiments was accomplished using a TESCAN MIRA3 FEG scanning electron microscope (SEM) at an accelerating voltage of 10 or 20 keV. For image analysis, at least 3 grains oriented with the  $\langle 011 \rangle$  direction normal to the surface were imaged using the same magnification, and ImageJ software was used for image segmentation to measure the number density, average diameter, and percent of total surface area of the  $\alpha$ -alumina patches at each oxidation time. Transmission electron microscopy (TEM) and atom probe tomography (APT) samples were prepared by a standard focused ion beam (FIB) lift-out technique using a Thermo Fisher Helios 650 NanoLab dual scanning electron microscope (SEM)/focused ion beam (FIB). TEM imaging and diffraction were done using a JEOL 2010F analytical electron microscope operated with an accelerating voltage of 200 keV, and additional imaging and energy dispersive spectroscopy (EDS) mapping and analysis were done using a JEOL 2100F scanning transmission electron microscope (STEM) equipped with an EDAX EDS detector and acquisition software, at an accelerating voltage of 200 keV. Atom probe tomography (APT) data collection was performed using a Cameca LEAP 5000HR instrument operated in laser pulsing mode with a pulse energy of 20–30 pJ, a pulse rate of 125 kHz, and a detection rate of 0.5%, with samples cooled to 50 K. APT data analysis was done using Cameca IVAS software, version 3.8.2.

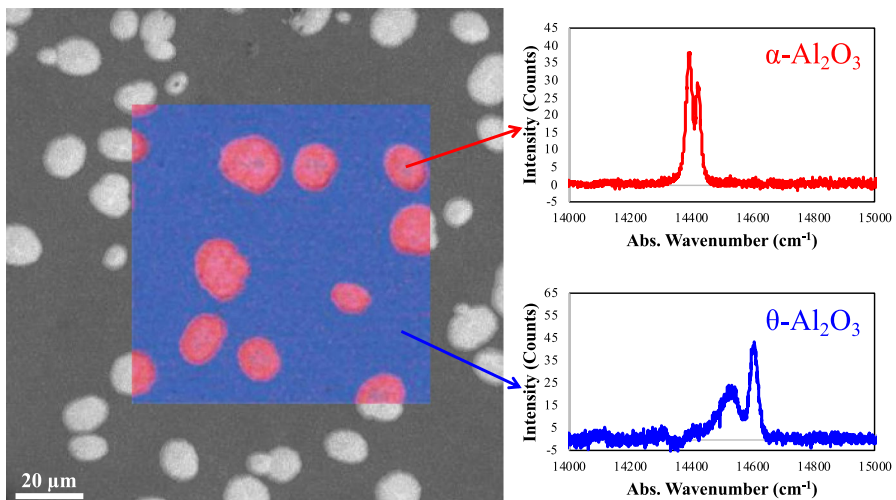


**Fig. 1** SEM surface image of the NiAlY alloy oxidized for 15 h at 950°C, with an overlaid PLS map. Luminescence spectra from the bright and dark regions are shown on the right. Peak positions in the spectra from the bright (red) regions were consistent with those of the  $\alpha$ - $\text{Al}_2\text{O}_3$  phase, while those in spectra from the dark (blue) region were consistent with those of the  $\theta$ - $\text{Al}_2\text{O}_3$  phase. (Color figure online)

## Results

To examine the nucleation and lateral growth behavior of  $\alpha\text{-Al}_2\text{O}_3$ , SEM imaging was used to characterize the surface microstructure, while correlative photoluminescence imaging allowed for  $\text{Al}_2\text{O}_3$  phase identification on the same area. At each oxidation time, ranging from 1 to 15 h of oxidation at 950 °C, bright circular “patches” could be seen using secondary electron imaging, while most of the surface was covered by an oxide that appeared darker. A representative image for the NiAlY alloy oxidized for 15 h is shown in Fig. 1. For all alloys, the surface topography of the darker phase appeared rougher than the bright patches, and the bright patches appeared smoother near their centers. Using PLS mapping (Fig. 1), the dark oxide exhibited fluorescence spectra with peaks consistent with those of the  $\theta\text{-Al}_2\text{O}_3$  phase (blue in PLS mapping), while the bright patches revealed fluorescence spectra consistent with those of the  $\alpha\text{-Al}_2\text{O}_3$  phase (red). The number density and shape of the  $\alpha\text{-Al}_2\text{O}_3$  patches were found to depend on substrate grain orientation, so the remainder of the results are presented only for  $\langle 011 \rangle$  orientated NiAl grains.

Surface SEM images were taken at progressing oxidation times for each alloy (Fig. 2) to compare their patch nucleation and growth behaviors. After one hour of oxidation, both Ti-containing alloys had a few larger  $\alpha\text{-Al}_2\text{O}_3$  patches and a higher number density of patches compared to the other alloys. Some of the larger

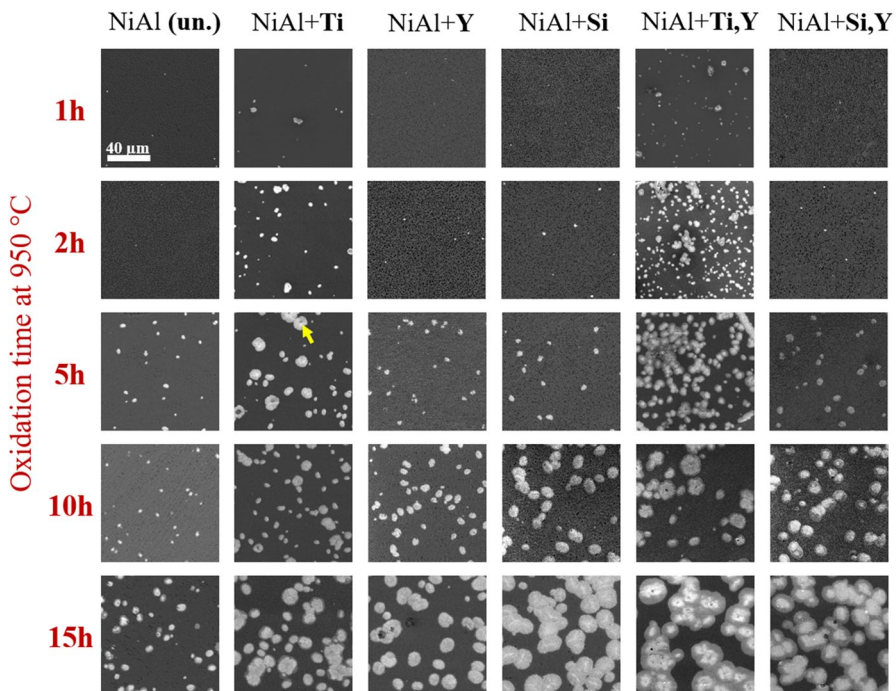


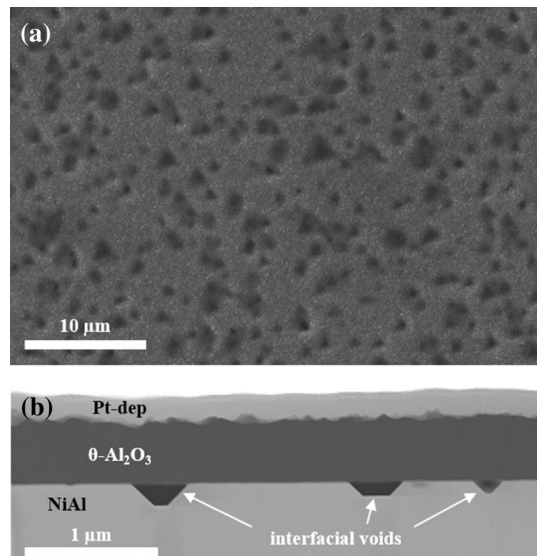
**Fig. 2** SEM surface images increasing oxidation exposures at 950°C from 1 to 15 h. The yellow arrow indicates a nodule of Ti-rich oxide at the center of one of the  $\alpha\text{-Al}_2\text{O}_3$  patches (Color figure online)

patches that had visibly cracked on the Ti-containing alloys often contained nodules of Ti-rich oxide at their centers (for example, NiAlTi at 5 h). These Ti-rich oxides were identified by EDS analysis. After 2 h of oxidation, no evolution was noted for the un-doped, Y- and Si-containing alloys. However, many more  $\alpha$ -Al<sub>2</sub>O<sub>3</sub> patches were present on the Ti-doped alloys. Some patches had grown larger compared to the patches observed after 1 h. After 5 h, a higher number density of patches as well as larger patches were noted for the un-doped, Y-, and Si-doped alloys compared to the observations at 1 and 2 h. Patches also continued to grow on the Ti-containing alloys. After 10 h, the un-doped and Y-doped alloys had the smallest patches, while the Si and Ti-containing alloys had larger, similarly sized patches. After 15 h the Y- and un-doped alloys again showed smaller patches than the other alloys. Patches on the Si- and Ti-containing alloys started to impinge upon each other due to continued growth.

Dark spots can be seen in the SEM images from 1 to 15 h of the un-doped, Y-, Si-, and SiY-doped alloys, but not on those of the Ti-containing alloys. The spots (Fig. 3a) are associated with faceted interfacial voids present at the oxide–metal interface, as evidenced via cross-sectional imaging (Fig. 3b). The number density and shape of the voids varied with alloy chemistry, grain orientation, and surface finish. No voids were observed on the Ti-containing alloys. On the un-doped, Y-, and Si-doped alloys, a higher density of voids was observed on  $\langle 111 \rangle$ -oriented NiAl grains, and on polishing scratches.

The qualitative  $\alpha$ -Al<sub>2</sub>O<sub>3</sub> patch nucleation and lateral growth behavior was further examined with quantitative image analysis of at least three  $\langle 011 \rangle$  grains from each alloy; results are summarized in Fig. 4. The overall transformation rate on each alloy was captured via the  $\alpha$ -Al<sub>2</sub>O<sub>3</sub> surface coverage (Fig. 4a). After 1 h only a small fraction of the alloy surfaces (less than 3%) had transformed to  $\alpha$ -Al<sub>2</sub>O<sub>3</sub>. By 5 h the  $\alpha$ -Al<sub>2</sub>O<sub>3</sub> surface coverage remained limited, but

**Fig. 3** **a** SEM surface image and **b** dark-field STEM image of the NiAl alloy oxidized for 10 h at 950°C



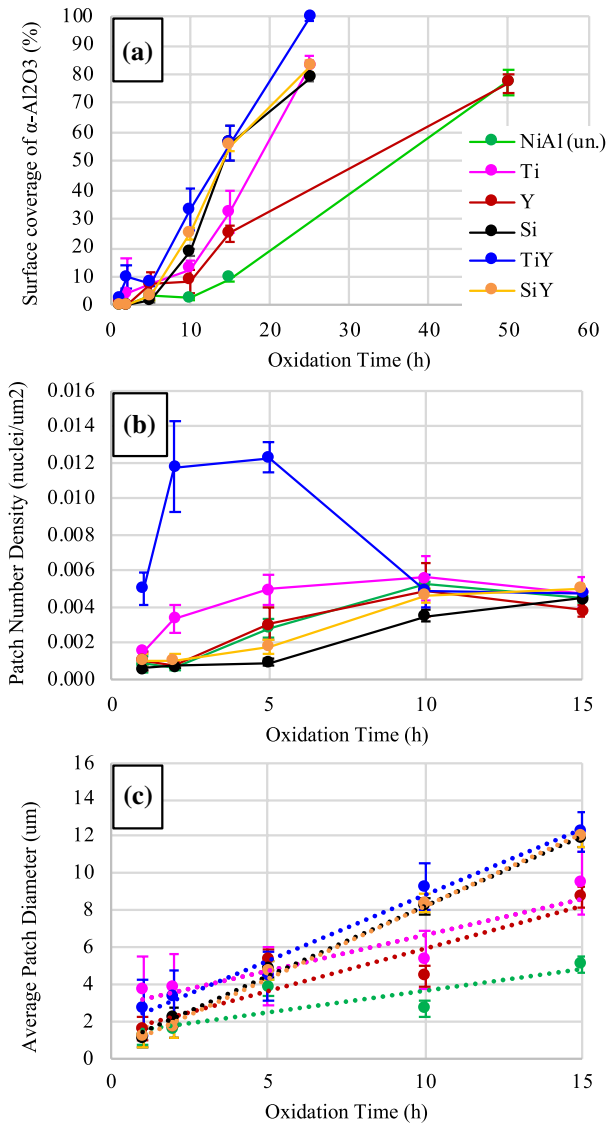


**Fig. 4** Summary of quantitative image analysis of surface SEM images showing **a** % of the surface covered by the  $\alpha$ -Al<sub>2</sub>O<sub>3</sub> phase, **b** number density of  $\alpha$ -Al<sub>2</sub>O<sub>3</sub> patches, and **c** average  $\alpha$ -Al<sub>2</sub>O<sub>3</sub> patch diameter, at consecutive oxidation exposures at 950 °C

was higher on the Ti-containing alloys (8–10%) than on the other alloys (<5%). After 10 h, the TiY and SiY co-doped alloys showed a significant increase in transformed area, 33 and 25%, respectively. The Si and Ti-doped alloys showed a lesser increase in surface coverage to ~19 and 13%, respectively. The un-doped and Y-doped alloy still had very low fractions of the total area transformed to  $\alpha$ -Al<sub>2</sub>O<sub>3</sub>, with <8% transformed after 10 h. By 25 h, the TiY-doped alloy was

nearly entirely transformed to  $\alpha$ -Al<sub>2</sub>O<sub>3</sub>. The Ti-, Si-, and SiY-doped alloys showed about 80% of the surface transformed to  $\alpha$ -Al<sub>2</sub>O<sub>3</sub>. Over twice the time (50 h) was needed for the un-doped and Y-doped alloys to exhibit similar 80%  $\alpha$ -Al<sub>2</sub>O<sub>3</sub> coverage. In summary, the transformation to  $\alpha$ -Al<sub>2</sub>O<sub>3</sub> occurred at a faster rate on Si- and Ti-containing alloys than on the un-doped and Y-doped alloys.

The  $\alpha$ -Al<sub>2</sub>O<sub>3</sub> nucleation behavior was inferred from the evolution of the number density of patches at consecutive oxidation times (Fig. 4b). The Ti- and TiY-doped alloys had significant early increase in the number densities of patches between 1 and 5 h. On the Ti-doped alloy, the patch number density then remained constant, suggesting that no significant additional nucleation took place. The TiY-doped alloy exhibited significantly higher nucleation density than the other alloys from 1 to 5 h, but then showed a decrease at 10 and 15 h to about the same level as the other alloys. The sudden decrease is not completely understood, but may be attributed to variability in the oxide grains examined or slight differences in oxidation conditions. Further work would be needed to confirm this unusual result. The number densities on the un-doped and Y-doped alloys steadily increased from 2 to 5 and 5 to 10 h, reaching comparable values as the Ti-containing alloys by 10 h. Finally, the Si-containing alloys showed delayed behavior with the most significant increases in the number densities between 5 and 10 h.

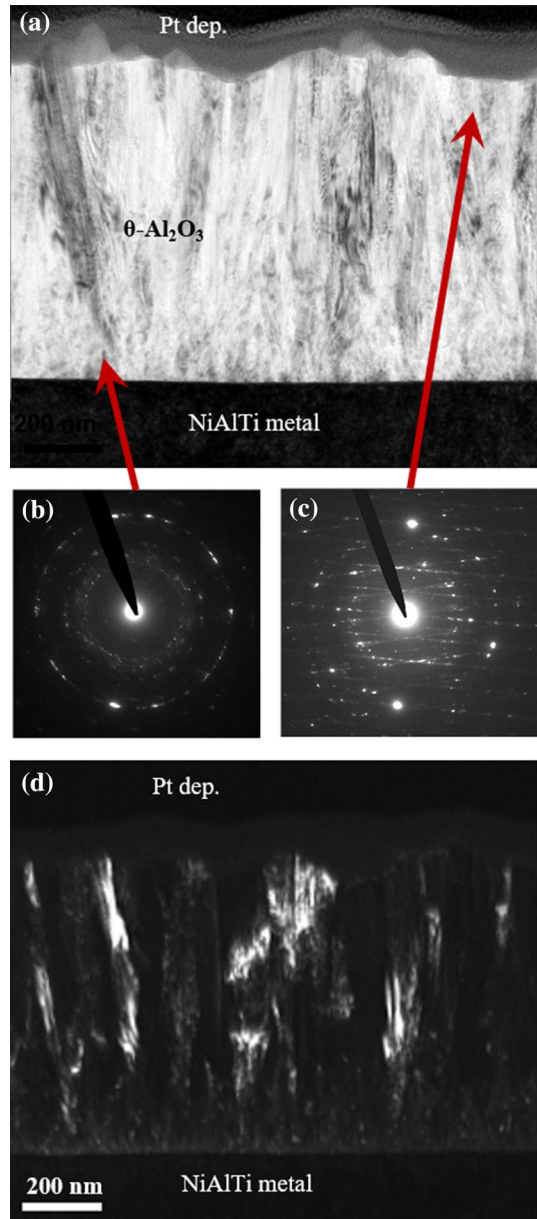
The lateral growth rate of  $\alpha$ -Al<sub>2</sub>O<sub>3</sub> was then compared for each alloy by measuring the average  $\alpha$ -Al<sub>2</sub>O<sub>3</sub> patch diameter at successive oxidation times (Fig. 4c). After 1 h, the Ti-containing alloys exhibited larger patches with diameters, around 4  $\mu$ m, compared to all other alloys with patch diameters around 1  $\mu$ m. As oxidation progressed, the average  $\alpha$ -Al<sub>2</sub>O<sub>3</sub> patch size on the Y-, and Ti-doped alloys increased slightly faster than that on the un-doped alloy. The Si- and TiY-doped alloys had significantly higher rates of lateral patch growth, and after 15 h, the Si-containing alloys and TiY-doped alloy had the largest  $\alpha$ -Al<sub>2</sub>O<sub>3</sub> patches compared to the other alloys. Consequently, Y, Ti, and Si increase lateral growth rate of  $\alpha$ -Al<sub>2</sub>O<sub>3</sub>, with Si exhibiting the strongest effect.

In the search for mechanisms explaining the changes in nucleation and growth rates, we hypothesized that the dopants may elicit differences in the  $\theta$ -Al<sub>2</sub>O<sub>3</sub> microstructure and/or the structure of the  $\theta$ - $\alpha$  transformation front. Cross-sectional TEM lift-outs were examined from each of the alloys on  $\langle 011 \rangle$ -oriented grains after 10 h of oxidation at 950°C. The  $\theta$ -Al<sub>2</sub>O<sub>3</sub> microstructure was found to be similar for all the alloys, and a representative bright-field STEM image is shown in Fig. 5a. Near the oxide–metal interface, the  $\theta$ -Al<sub>2</sub>O<sub>3</sub> was observed to consist of a layer of discrete, nano-crystalline grains, as evidenced by the rings in the diffraction pattern (Fig. 5b) that were consistent with the d-spacing of the  $\theta$ -Al<sub>2</sub>O<sub>3</sub> phase. Toward the surface of the  $\theta$ -Al<sub>2</sub>O<sub>3</sub> layer, elongated lathe-like grains were visible. A diffraction pattern from this region (Fig. 5c) showed textured rings that had d-spacings consistent with  $\theta$ -Al<sub>2</sub>O<sub>3</sub>, and contained streaking perpendicular to the lathes. Spacing between the streaks was consistent with the d-spacing in the  $\langle 001 \rangle$  direction of the  $\theta$ -Al<sub>2</sub>O<sub>3</sub> phase. Both the nano-crystalline grains and lathe-like grains can be seen clearly in the dark-field STEM image shown in Fig. 5d.

While the  $\theta$ -Al<sub>2</sub>O<sub>3</sub> layer exhibited comparable microstructure, its thickness varied with alloy composition. Figure 6 shows a comparison of the  $\theta$ -Al<sub>2</sub>O<sub>3</sub> layer on



**Fig. 5** NiAlTi alloy oxidized for 10 h at 950 °C. **a** Bright-field image of the  $\theta$ -Al<sub>2</sub>O<sub>3</sub> layer in cross-section. **c** Selected area diffraction pattern from a region near the  $\theta$ -Al<sub>2</sub>O<sub>3</sub>-metal interface. **d** Selected area diffraction pattern from a region near the  $\theta$ -Al<sub>2</sub>O<sub>3</sub> layer surface. **b** Dark-field TEM image of the same area



the un-doped, Ti-, Y-, and Si-doped alloys, along with a plot of the  $\theta$ -Al<sub>2</sub>O<sub>3</sub> thickness. The Si- and SiY-doped alloys exhibited the thickest  $\theta$ -Al<sub>2</sub>O<sub>3</sub> layers, followed in decreasing thickness by the TiY-, Y-, Ti-, and un-doped alloys.

The growth of the  $\alpha$ -Al<sub>2</sub>O<sub>3</sub> through the  $\theta$ -Al<sub>2</sub>O<sub>3</sub> layer in cross-section was similar for all of the alloys. A representative cross-section through an  $\alpha$ -Al<sub>2</sub>O<sub>3</sub> patch on the TiY-doped alloy is shown in Fig. 7. Diffraction patterns from the bright grain visible

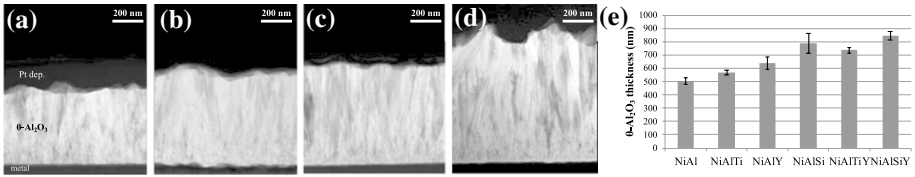


**Fig. 6** Bright-field TEM images of the  $\theta$ - $\text{Al}_2\text{O}_3$  layer in cross-section on the **a** NiAl, **b** NiAlTi, **c** NiAlY, and **d** NiAlSi alloys oxidized for 10 h at 950°C. **e**  $\theta$ - $\text{Al}_2\text{O}_3$  layer thicknesses after 10 h of oxidation at 950°C

at the right of the image were consistent with the  $\alpha$ - $\text{Al}_2\text{O}_3$  phase and revealed that the patch had nucleated and grown as a single crystal. In some cases, on patches which had already cracked, grain boundaries could be observed, resulting in slightly misoriented  $\alpha$ - $\text{Al}_2\text{O}_3$  sub-grains. On all alloys, the  $\alpha$ - $\text{Al}_2\text{O}_3$  patches were slightly wider laterally near the top surface of the scale than at the oxide–metal interface. In the surface SEM images (Fig. 2), the slightly darker contrast visible around the edge of some of the patches (for example NiAlTiY at 15 h) is thought to be the result of both  $\theta$ - and  $\alpha$ - $\text{Al}_2\text{O}_3$  present through the scale thickness, thus giving different contrast in SEM than the patch centers, which consisted entirely of  $\alpha$ - $\text{Al}_2\text{O}_3$ . The  $\alpha$ - $\text{Al}_2\text{O}_3$  patches were also observed to be thinner in cross-section near their centers than at the patch edges due to both volume contraction and slower growth rate of the  $\alpha$ - $\text{Al}_2\text{O}_3$  phase compared to  $\theta$ - $\text{Al}_2\text{O}_3$ .

Observing that  $\theta$ - and  $\alpha$ - $\text{Al}_2\text{O}_3$  microstructure was similar for each of the alloys, we next examined potential differences in chemistry of the alumina scales. Using STEM-EDS mapping, no detectable levels of Y, Ti, and Si were observed in either the  $\theta$ - or  $\alpha$ - $\text{Al}_2\text{O}_3$  phase. APT analyses also showed Ti and Y levels that were below the instrument detection level in both the  $\theta$ - and  $\alpha$ - $\text{Al}_2\text{O}_3$  phase. EDS maps were also collected on several areas that included the  $\theta$ - $\text{Al}_2\text{O}_3$  layer, the  $\theta$ / $\alpha$ - $\text{Al}_2\text{O}_3$  interface, and the oxide–metal interface under both the  $\theta$ - and  $\alpha$ - $\text{Al}_2\text{O}_3$  on each alloy. No Y or Si segregation was observed at any of the interfaces. On the Ti- and TiY-doped alloys, however, a somewhat continuous layer of Ti-segregation at the oxide–metal interface was observed after a short 30-min exposure (Fig. 8). After 10 h, discrete Ti-rich regions were observed at the oxide–metal interface under both the  $\theta$ - and  $\alpha$ - $\text{Al}_2\text{O}_3$ , shown in Fig. 9.

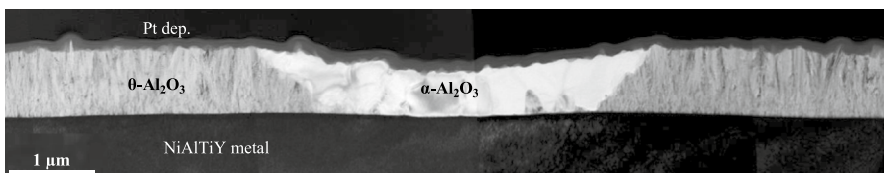


**Fig. 7** Bright-field cross-sectional TEM image of the NiAlTiY alloy oxidized for 10 h at 950°C showing the  $\theta$ - $\text{Al}_2\text{O}_3$  layer and an  $\alpha$ - $\text{Al}_2\text{O}_3$  patch

## Discussion

It is well established that dopant elements can significantly reduce the oxidation rate of alumina-forming alloys. The majority of the prior studies on this topic focused on the effect of dopants on the steady-state oxidation stage, i.e. changes in Al and O transport along the grain boundaries during oxidation. However, as demonstrated here and in previous literature, e.g. [15, 16], dopants also can have significant effects on the transient oxidation stage. The prolonged growth of metastable alumina in the transient stage can deplete the alloy of aluminum, a significant problem for thin-walled components at intermediate temperatures ( $\sim 800$ – $1000^\circ\text{C}$ ) [30]. Thus, understanding how various dopants change the length of transient oxidation is of technological importance.

The overall oxide morphology and its evolution with time observed in this study are consistent with literature on the transient oxidation of NiAl alloys [6, 11, 26, 31]. An initial metastable alumina layer precedes the nucleation and radial growth

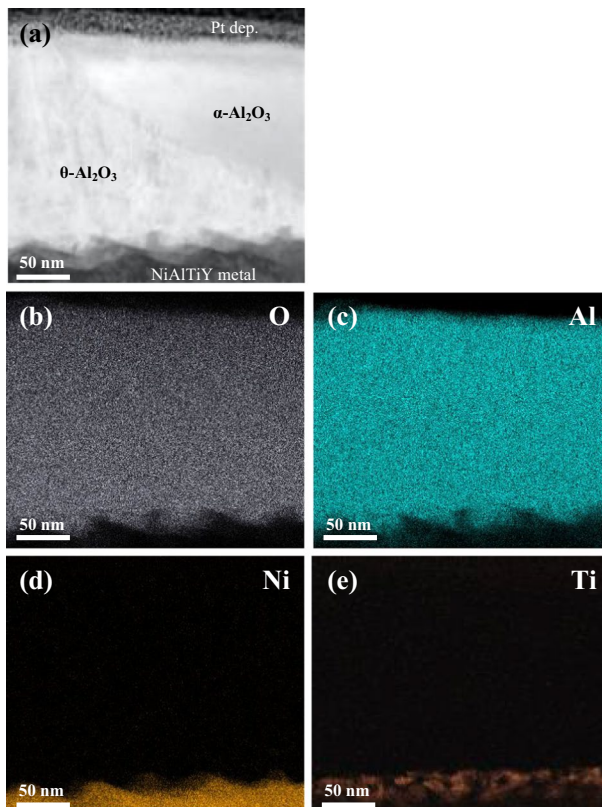


**Fig. 8** STEM-EDS maps of the NiAlTiY alloy oxidized for 30 min at  $950^\circ\text{C}$ . **a** Bright-field STEM image of the  $\theta$ - $\alpha\text{-Al}_2\text{O}_3$  interface, with corresponding elemental maps showing the distribution of **b** oxygen, **c** aluminum, **d** nickel, **e** titanium

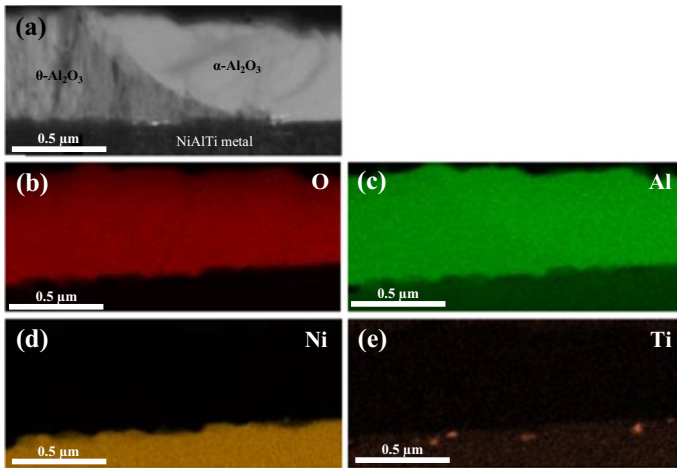


**Fig. 9** STEM-EDS maps of the NiAlTi alloy oxidized for 10 h at 950 °C. **a** Bright-field STEM image of the  $\theta$ - $\alpha$ - $\text{Al}_2\text{O}_3$  interface, with corresponding elemental maps showing the distribution of **b** oxygen, **c** aluminum, **d** nickel, **e** titanium

of  $\alpha$ - $\text{Al}_2\text{O}_3$ . The initial  $\theta$ - $\text{Al}_2\text{O}_3$  layer has a rough, blade-like appearance due to the rapid outward growth of the metastable phase [7, 8, 32]. When the transformation to  $\alpha$ - $\text{Al}_2\text{O}_3$  occurs, the rapid outward growth of  $\theta$ - $\text{Al}_2\text{O}_3$  ceases and surface diffusion smooths out the blade-like topology [11, 33]. Thus,  $\alpha$ - $\text{Al}_2\text{O}_3$  patches within the  $\theta$ - $\text{Al}_2\text{O}_3$  layer are smoother near their centers where the transformation to  $\alpha$ - $\text{Al}_2\text{O}_3$  first takes place.

While the scales on all the NiAl alloys shared these common features, they also differed by the nucleation and growth rates of the  $\alpha$ - $\text{Al}_2\text{O}_3$  patches. The present results suggest that Ti and Si accelerate the transformation, in agreement with prior literature [15, 18–21]. Our findings also suggest that Y has minimal effect on the transformation, contrary to prior results [12, 15–17]. Since the rate of transformation of the  $\theta$ - $\text{Al}_2\text{O}_3$  layer to a fully  $\alpha$ - $\text{Al}_2\text{O}_3$  scale is controlled by the nucleation and the lateral growth rate of  $\alpha$ - $\text{Al}_2\text{O}_3$  patches, it is worth noting that dopants affect nucleation and growth differently.

Si retards the onset of nucleation and accelerates lateral growth. The longer incubation time in the presence of Si is consistent with Si acting to stabilize the metastable  $\text{Al}_2\text{O}_3$  phase and decrease the driving force of the  $\theta$ - $\alpha$  transformation [34, 35]. Because Si-containing alloys exhibited the thickest  $\theta$ - $\text{Al}_2\text{O}_3$  layers, Si also accelerated the growth of  $\theta$ - $\text{Al}_2\text{O}_3$ , which is dominated by the outward diffusion of Al cations [32]. Though studies of defect levels in  $\theta$ - $\text{Al}_2\text{O}_3$  could not be found, prior work showed that minute levels of dopants can dramatically affect the concentration of intrinsic defects in  $\alpha$ - $\text{Al}_2\text{O}_3$  [36]. Similarly, if  $\text{Si}^{4+}$  cation substitutes for  $\text{Al}^{3+}$  in the  $\theta$ - $\text{Al}_2\text{O}_3$  phase [34], charge neutrality would require additional cation vacancies to form, promoting faster diffusion of Al cations than in un-doped  $\theta$ - $\text{Al}_2\text{O}_3$ , and explaining the faster outward growth of the  $\theta$ - $\text{Al}_2\text{O}_3$  layer observed on the Si-doped alloy. A significant assumption here is the presence of Si in the scale, which we

could not confirm. Nonetheless, the increased concentration of cation vacancies in the Si-doped scale could conceivably accelerate the transformation from  $\theta$ - to  $\alpha$ -Al<sub>2</sub>O<sub>3</sub>, since the transformation is diffusion-controlled [37, 38] and involves the structural re-arrangement of Al atoms [39, 40].

Ti and Y also have a slight tendency to accelerate lateral growth, but TiY-doping had a significant effect. The slight acceleration of the lateral  $\alpha$ -Al<sub>2</sub>O<sub>3</sub> growth in the presence of Y or Ti compared to Si may be due to smaller changes in the cation vacancy concentration, which are less expected for Y and Ti since large Y<sup>3+</sup> ions typically substitute for Al<sup>3+</sup> with the same charge state, and Ti can coexist as Ti<sup>4+</sup> or Ti<sup>3+</sup> in alumina depending on the oxygen partial pressure [41, 42]. The significant effect of co-doping with Ti + Y on lateral  $\alpha$ -Al<sub>2</sub>O<sub>3</sub> growth is not understood at present. However, the TiY-doped alloy, like the Si-containing alloys, had a thicker  $\theta$ -Al<sub>2</sub>O<sub>3</sub> layer than the undoped alloy. Therefore, co-doping accelerated both  $\theta$ -Al<sub>2</sub>O<sub>3</sub> growth and the  $\theta$ - $\alpha$  transformation, suggestive of a mechanism involving defect concentrations.

Unlike Si, Ti appears to promote early nucleation. After just 30 min, a Ti-rich layer was observed at the alumina-metal interface of the TiY-doped alloy. It may be a thin Ti-based oxide phase because of the presence of an oxidizing atmosphere; however, it was not confirmed. One possible explanation is that the Ti oxide layer functioned as a seed layer for  $\alpha$ -Al<sub>2</sub>O<sub>3</sub>, promoting  $\alpha$ -Al<sub>2</sub>O<sub>3</sub> nucleation. Such template layers have previously been reported for Cr- and Fe-containing alloys [6, 43, 44] that can form an initial layer of (Cr,Fe)<sub>2</sub>O<sub>3</sub> that is isostructural with Al<sub>2</sub>O<sub>3</sub>. In the present case, Ti<sub>2</sub>O<sub>3</sub> is isostructural with Al<sub>2</sub>O<sub>3</sub>; however, other Ti oxide phases could form as well, so further evidence is needed to support this mechanism. At longer oxidation times the continuous Ti-rich layer is no longer observed, possibly due to its destabilization and incorporation into the thickening Al<sub>2</sub>O<sub>3</sub> layer. The disappearance of the Ti-rich layer is also consistent with a decrease in the nucleation rate at longer oxidation times.

An additional feature of the Ti-containing alloys was the absence of interfacial voids. Faceted interfacial voids have been widely observed upon the oxidation of NiAl alloys and are thought to occur by vacancy injection and coalescence [26, 31, 45–47]. As aluminum selectively oxidizes to form Al<sub>2</sub>O<sub>3</sub>, the alloy becomes depleted of Al, while vacancies are formed at the oxide–metal interface. The resulting surplus nickel at the oxide–metal interface diffuses back into the alloy, leaving additional vacancies at the interface. For Al-lean NiAl alloys, the diffusivity of nickel is larger than that of aluminum [48] and the flux of Ni back into the alloy exceeds that of Al. This flux imbalance allows vacancies to coalesce into large interfacial cavities underneath the rigid surface oxide [45]. There are several possible mechanisms by which Ti may be suppressing these interfacial voids. Ti additions in NiAl may change the diffusivity of Ni or Al such that they are approximately equal, i.e. increasing the diffusivity of Al or decreasing the diffusivity of Ni. In Pt-containing NiAl for example, Pt suppresses interfacial void formation by increasing the aluminum diffusivity [49]. In the case of Ti addition, no evidence from literature could be found suggesting that Ti alters the Al or Ni diffusivity. Using wavelength dispersive spectroscopy (WDS), we also verified that the depletion distance of Al beneath the scale was essentially the same on the un-doped and the Ti-doped NiAl

alloys. From the oxide thickness observations, Ti is also not reducing the growth rate of  $\theta$ - $\text{Al}_2\text{O}_3$ , which would reduce the formation of vacancies at the scale-alloy interface. A possible explanation for the lack of voids comes from the observation of the Ti-rich layer at early oxidation times. Under the assumption that this layer is a Ti-based oxide, its formation would be accompanied by an increase in volume [50, 51]. Vacancies at the oxide-metal interface formed during the growth of  $\text{Al}_2\text{O}_3$  could conceivably be annihilated upon the formation of the Ti-based oxide layer at the interface.

Y had no conclusive effect on alumina transformation, in contrast with previous literature reporting that Y hinders the metastable  $\text{Al}_2\text{O}_3$  to  $\alpha$ - $\text{Al}_2\text{O}_3$  transformation [12, 15–17]. The majority of these studies, however, utilized either implanted Y or larger alloying additions of Y in comparison with the current study, which could explain the lack of any obvious effect. The alloys co-doped with Ti + Y and Si + Y behaved similarly to the single-doped Ti- and Si-doped alloys, respectively, consistent with the observation that the Y-addition had little effect on the  $\theta$ - to  $\alpha$ - $\text{Al}_2\text{O}_3$  transformation.

## Conclusions

We presented results that clarify the effect of several dopant elements on the nucleation and growth behavior during transient stage alumina phase transformation. The following conclusions were reached:

- Ti, Si, and Y doping had no observable effect on the microstructure of the  $\theta$ - $\text{Al}_2\text{O}_3$  layer.
- Doping NiAl with Ti accelerated the  $\theta$  to  $\alpha$  alumina transformation by reducing the incubation time for nucleation and increasing nucleation rate.
- On the Ti-containing alloys, a Ti-rich layer was detected at the oxide-metal interface at the shortest oxidation times, but no segregation or partitioning of the dopants was otherwise observed.
- Doping NiAl with Ti suppressed interfacial void formation.
- Doping NiAl with Si accelerated the  $\theta$  to  $\alpha$  alumina transformation by accelerating the lateral growth rate of  $\alpha$ - $\text{Al}_2\text{O}_3$ , despite slightly increasing the incubation time for nucleation compared to the un-doped alloy.
- Ti, Si, and Y doping accelerated the outward growth of  $\theta$ - $\text{Al}_2\text{O}_3$ , with Si having the most significant effect.
- The addition of Y had little effect on the overall transformation rate.
- Co-doping with Ti + Y accelerated the overall transformation to  $\alpha$ - $\text{Al}_2\text{O}_3$  by increasing both nucleation rate and lateral growth rate of  $\alpha$ - $\text{Al}_2\text{O}_3$ .
- Co-doping with Si + Y had no additional effect on the transformation rate compared to doping only with Si.

Finally, our results indicate that the length of transient oxidation can be tuned with the addition of various dopant elements. This has implications for both alloy

design and modelling oxidation kinetics. Understanding how certain dopants reduce the length of transient oxidation may enable the design of alloys that quickly form a protective  $\alpha$ -Al<sub>2</sub>O<sub>3</sub> scale over a range of temperatures. Measurements of nucleation and lateral growth rate of  $\alpha$ -Al<sub>2</sub>O<sub>3</sub> during transient oxidation are needed to develop more accurate predictive models of oxidation kinetics and component lifetime. Future work is underway to ascertain any relationship between behavior during transient oxidation, steady-state scale microstructure and grain size, and steady-state oxidation kinetics.

**Acknowledgements** This work was supported by the National Science Foundation (NSF) through Grant # DMR-1352157. The authors gratefully acknowledge financial and technical support from the University of Michigan Center for Materials Characterization.

## References

1. T.M. Pollock and S. Tin, *Nickel-Based Superalloys for Advanced Turbine Engines: Chemistry, Microstructure, and Properties*. Journal of Propulsion and Power, 2006. **22**(2): p. 361-374.
2. H. Long, et al., *Microstructural and compositional design of Ni-based single crystalline superalloys-- A review*. Journal of Alloys and Compounds, 2018. **743**: p. 203-220.
3. C.L. Angerman, *Long-Term Oxidation of Superalloys*. Oxidation of Metals, 1972. **5**(2): p. 149-167.
4. N. Birks, G.H. Meier, and F.S. Pettit, *Introduction to the High-Temperature Oxidation of Metals*. 2006: Cambridge University Press.
5. J.K. Doychak and T.E. Mitchell. *High Temperature Oxidation of beta-NiAl*. in *Materials Research Society Symposium*. 1985.
6. M.W. Brumm and H.J. Grabke, *The Oxidation Behaviour of NiAl-- I. Phase Transformations in the Alumina Scale During Oxidation of NiAl and NiAl-Cr Alloys*. Corrosion Science, 1992. **33**(11): p. 1677–1690.
7. J. Doychak, J.L. Smialek, and T.E. Mitchell, *Transient Oxidation of Single-Crystal B-NiAl*. Metallurgical Transactions A, 1989. **20A**: p. 499-518.
8. J.C. Yang, et al., *Transient Oxidation of NiAl*. Acta Materialia, 1998. **46**(6): p. 2195-2201.
9. P.Y. Hou, A.P. Paulikas, and B.W. Veal, *Stress development and relaxation in Al<sub>2</sub>O<sub>3</sub> during early stage oxidation of B-NiAl*. Materials at High Temperatures, 2005. **22**(3/4): p. 535-543.
10. G.C. Rybicki and J.L. Smialek, *Effect of the theta-alpha-Al<sub>2</sub>O<sub>3</sub> Transformation on the Oxidation Behavior of beta-NiAl+Zr*. Oxidation of Metals, 1989. **31**(3/4): p. 275-304.
11. V.K. Tolpygo and D.R. Clarke, *Microstructural study of the theta-alpha transformation in alumina scales formed on nickel-aluminides*. Materials at High Temperatures, 2000. **17**(1): p. 59-70.
12. H.J. Choi, et al., *Transmission electron microscopy observations on the phase composition and microstructure of the oxidation scale grown on as-polished and yttrium-implanted B-NiAl*. Surface and Coatings Technology, 2010. **205**: p. 1206-1210.
13. H. Hindam and D.P. Whittle, *Microstructure, Adhesion and Growth Kinetics of Protective Scales on Metals and Alloys*. Oxidation of Metals, 1982. **18**(5/6): p. 245-284.
14. D.P. Whittle and J. Stringer, *Improvement in high temperature oxidation resistance by additions of reactive elements or oxide dispersions*. Philosophical Transactions of the Royal Society of London, Series A, 1980. **295**: p. 309-329.
15. B.A. Pint, M. Treska, and L.W. Hobbs, *The Effect of Various Oxide Dispersions on the Phase Composition and Morphology of Al<sub>2</sub>O<sub>3</sub> Scales Grown on B-NiAl*. Oxidation of Metals, 1997. **47**(1/2): p. 1-20.
16. I. Rommerskirchen and V. Kolarik, *Oxidation of B-NiAl, undoped and doped with Ce, Y, Hf*. Materials and Corrosion, 1996. **47**: p. 625-630.
17. D.D. Ragan, T. Mates, and D.R. Clarke, *Effect of Yttrium and Erbium Ions on Epitaxial Phase Transformations in Alumina*. Journal of the American Ceramic Society, 2003. **86**(4): p. 541-545.

18. W. Fei, S.C. Kuiry, and S. Seal, *Inhibition of Metastable Alumina Formation on Fe-Cr-Al-Y Alloy Fibers at High Temperature using Titania Coating* Oxidation of Metals, 2004. **62**(1/2): p. 29-44.
19. E. N'Dah, et al., *Metastable alumina formation during oxidation of FeCrAl and its suppression by surface treatments*. Materials and Corrosion, 2005. **56**(12): p. 843-847.
20. J. He, et al., *The role of Cr and Si in affecting high-temperature oxidation behaviour of minor Dy doped NiAl alloys*. Corrosion Science, 2013. **77**: p. 322-333.
21. P. Dai, et al., *The effect of silicon on the oxidation behavior of NiAlHf coating system*. Applied Surface Science, 2013. **271**: p. 311-316.
22. R. Munoz-Arroyo, et al., *Influence of Composition and Phase Distribution on the Oxidation Behaviour of NiCoCrAlY Alloys*. Materials Science Forum, 2001. **369-372**: p. 165-172.
23. W. Zhao, Z. Li, and B. Gleeson, *A New Kinetics-Based Approach to Quantifying the Extent of Metastable-Stable Phase Transformation in Thermally-Grown Al<sub>2</sub>O<sub>3</sub> Scales*. Oxidation of Metals, 2013. **79**: p. 361-381.
24. X. Liang and X. Wang, *Modeling of theta-alpha alumina lateral phase transformation with applications to oxidation kinetics of NiAl-based alloys*. Materials and Design, 2016. **112**: p. 519-529.
25. J. Jedlinski, et al., *Oxide phases and residual stresses in scales formed at early stages of oxidation of B-NiAl at 1473K and the effect of implanted yttrium*. Materials and Corrosion, 2017. **68**(2): p. 235-248.
26. H.M. Hindam and W.W. Smeltzer, *Growth and Microstructure of alpha-Al<sub>2</sub>O<sub>3</sub> on beta-NiAl*. Journal of the Electrochemical Society: Solid State Science, 1980. **127**(7): p. 1630-1635.
27. J. Doychak and M. Ruhle, *TEM Studies of Oxidized NiAl and Ni<sub>3</sub>Al Cross Sections*. Oxidation of Metals, 1989. **31**(5/6): p. 431-452.
28. D.M. Lipkin and D.R. Clarke, *Measurement of the Stress in Oxide Scales Formed by Oxidation of Alumina-Forming Alloys*. Oxidation of Metals, 1996. **45**(3/4): p. 267-280.
29. Q. Wen, D.M. Lipkin, and D.R. Clarke, *Luminescence Characterization of Chromium-Containing theta-Alumina*. Journal of the American Ceramic Society, 1998. **81**(12): p. 3345-3348.
30. D. Naumenko, et al., *Parameters affecting transient oxide formation on FeCrAl based foil and fibre materials*. Materials at High Temperatures, 2003. **20**(3): p. 287-293.
31. J. Smialek, *Oxide Morphology and Spalling Model for NiAl*. Metallurgical Transactions A, 1978. **9A**: p. 309-320.
32. B.A. Pint, J.R. Martin, and L.W. Hobbs, *The oxidation mechanism of theta-Al<sub>2</sub>O<sub>3</sub> scales*. Solid State Ionics, 1995. **78**: p. 99-107.
33. J.K. Doychak, *The Evolution and Growth of Al<sub>2</sub>O<sub>3</sub> Scales on beta-NiAl*, in *Department of Metallurgy and Materials Science*. 1986, Case Western Reserve University: Cleveland, OH. p. 242.
34. E. Wallin, et al., *Effects of additives in alpha and theta-alumina: an ab initio study*. Journal of Physics: Condensed Matter, 2004. **16**: p. 8971-8980.
35. H. Bolvardi, et al., *Effect of Si additions on the thermal stability and the phase transition sequence of sputtered amorphous alumina thin films*. Journal of Applied Physics, 2015. **117**: p. 1-22.
36. K.P.D. Lagerlof and R.W. Grimes, *The Defect Chemistry of Sapphire (α-Al<sub>2</sub>O<sub>3</sub>)*. Acta Materialia, 1998. **46**(16): p. 5689-5700.
37. R.B. Bagwell, G.L. Messing, and P.R. Howell, *The formation of alpha-Al<sub>2</sub>O<sub>3</sub> from theta-Al<sub>2</sub>O<sub>3</sub>: The relevance of a "critical size" and: Diffusional nucleation or "synchro-shear"?* Journal of Materials Science, 2001. **36**: p. 1833-1841.
38. P. Burtin, et al., *Influence of Surface Area and Additives on the Thermal Stability of Transition Alumina Catalyst Supports. II: Kinetic Model and Interpretation*. Applied Catalysis, 1987. **34**: p. 239-254.
39. C.K. Loong, J.W.R. Jr., and M. Ozawa, *Structural phase transformations of rare-earth modified transition alumina to corundum*. Journal of Alloys and Compounds, 1997. **250**: p. 356-359.
40. I. Levin, et al., *Cubic to Monoclinic Phase Transformations in Alumina*. Acta Materialia, 1997. **45**(9): p. 3659-3669.
41. S.K. Mohapatra and F.A. Kroger, *Defect Structure of α-Al<sub>2</sub>O<sub>3</sub> Doped with Titanium*. Journal of the American Ceramic Society, 1977. **60**(9-10): p. 381-387.
42. K. Matsunaga and A. Nakamura, *First-principles study of defect energetics in titanium-doped alumina*. Physical Review B, 2003. **68**: p. 1-8.
43. J.M. Andersson, et al., *Microstructure of α-alumina thin films deposited at low temperatures on chromia template layers*. Journal of Vacuum Science and Technology, 2004. **22**(1): p. 117-121.



44. D. Renusch, et al., *Strain Determination in Thermally-Grown Alumina Scales Using Fluorescence Spectroscopy*. Oxidation of Metals, 1997. **48**(5/6): p. 471-495.
45. M.W. Brumm and H.J. Grabke, *Oxidation Behavior of NiAl-- II. Cavity Formation Beneath the Oxide Scale on NiAl of Different Stoichiometries*. Corrosion Science, 1993. **34**(4): p. 547–561.
46. F. Gesmundo and P.Y. Hou, *Analysis of Pore Formation at Oxide-Alloy Interfaces-- II. Theoretical Treatment of Vacancy Condensation for Immobile Interfaces*. Oxidation of Metals, 2003. **59**(1/2): p. 63–81.
47. H. Svensson, P. Knutsson, and K. Stiller, *Formation and Healing of Voids at the Metal-Oxide Interface in NiAl Alloys*. Oxidation of Metals, 2009. **71**: p. 143-156.
48. S. Shankar and L.L. Seigle, *Interdiffusion and Intrinsic Diffusion in the NiAl Phase of the Al-Ni System*. Metallurgical Transactions A, 1978. **9A**: p. 1467-1476.
49. H. Svensson, et al., Influence of Pt on the metal-oxide interface during high temperature oxidation of NiAl bulk materials. Corrosion Science, 2009. **51**: p. 539-546.
50. B. Xu, et al., *Structures, preparation and applications of titanium suboxides*. RSC Advances, 2016. **6**: p. 79706-79722.
51. N. Rahimi, R.A. Pax, and E.M. Gray, *Review of functional titanium oxides*. Progress in Solid State Chemistry, 2016. **44**: p. 86-105.

**Publisher's Note** Springer Nature remains neutral with regard to jurisdictional claims in published maps and institutional affiliations.